RSC Advances

ROYAL SOCIETY OF CHEMISTRY

www.rsc.org/advances

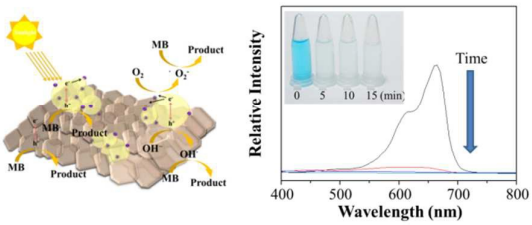

Sunlight-induced photocatalytic activity using $Ag/Ag_3PO_4/BiPO_4$

Journal Name

RSCPublishing

ARTICLE

Synthesis, Characterization, Enhanced Sunlight Photocatalytic Properties, and Stability of Ag/Ag_3PO_4 Nanostructure-Sensitized $BiPO_4$

Cite this: DOI: 10.1039/xoxxoooooox

Received ooth January 2012,
Accepted ooth January 2012

DOI: 10.1039/xoxxoooooox

www.rsc.org/

Tzu-Yun Huang[a], Yen-Jui Chen[a], Chi-Yung Lai[b] and Yang-Wei Lin[a,*]

This novel Ag/Ag_3PO_4 nanostructure-sensitized $BiPO_4$ ($Ag/Ag_3PO_4/BiPO_4$) photocatalyst was synthesized using hydrothermal and impregnation processes. Powder X-ray diffraction, UV–Vis diffuse reflectance spectroscopy, Raman spectroscopy, IR spectroscopy, X-ray photoelectron spectroscopy, transmission electron microscopy, and scanning electron microscopy were used to characterize the as-prepared products. The optical properties and morphology of $BiPO_4$ exhibited drastic changes and were dependent on the $AgNO_3$ concentration. Regarding methylene blue (MB), rhodamine B, and methyl orange degradation under solar irradiation (95% degradation within 5 min), $15\%Ag/Ag_3PO_4/BiPO_4$ exhibited considerably higher photocatalytic activity than did $BiPO_4$ and P25. After five cycles, $Ag/Ag_3PO_4/BiPO_4$ exhibited no apparent loss of activity, confirming its stability despite recycling. The practicality of this $Ag/Ag_3PO_4/BiPO_4$ was validated according to its ability to degrade MB in seawater, pond water, and industrial wastewater samples, which also demonstrated the advantages of its high photocatalytic activity. Moreover, $15\%Ag/Ag_3PO_4/BiPO_4$ also showed sunlight-induced photocatalytic disinfection activity toward *E. coli* cells. The enhanced photocatalytic activity and improved stability of $Ag/Ag_3PO_4/BiPO_4$ could be attributed to the strong visible light absorption by Ag/Ag_3PO_4 nanostructures, a low electron–hole recombination rate, and the highly efficient separation of photogenerated electron–hole pairs throughout $Ag_3PO_4/BiPO_4$ heterostructures. Moreover, holes were the main reactive species.

Introduction

Dyes are used in many industries for coloring products. However, most dyestuffs do not bind to product surfaces and are thus discharged into wastewater. Because of the chemical stability of dyes, conventional methods for mitigating this type of wastewater pollution are limited to decolorization of dyes. Photocatalysis has been extensively studied and applied as an effective technology for treating wastewater containing organic dyes.[1] For example, TiO_2, a heterogeneous photocatalyst, is considered attractive because of its wide availability, low cost, nontoxicity, and relatively high chemical stability.[2, 3] However, the photocatalytic activity of TiO_2 is insufficient for industrial applications because the high recombination rate of the photogenerated electrons and holes leads to high running costs.[4] Therefore, developing photocatalytic materials that are more efficient is urgently required.

Some novel materials, such as Bi- and V-based photocatalysts, have been synthesized in 2014 for finding materials with superior photocatalytic activity.[5-9] Among them, $BiPO_4$ has unique catalytic applications. Many systematic studies have analyzed the morphology-dependent photocatalytic activity, recyclability, and practicability of these catalysts.[10, 11] The high photocatalytic activity of $BiPO_4$ was primarily attributed to the high energy of the valence band and high separation efficiency of electron–hole pairs.[12, 13] However, poor solar efficiency hindered the applicability of $BiPO_4$. Therefore, developing photocatalysts that have high reactivity under visible light irradiation is crucial for overcoming the drawbacks of $BiPO_4$. Recently, Ag_3PO_4 was found to demonstrate high performance in the photodecomposition of organic dyes in wastewater under visible light illumination.[14, 15] However, Ag_3PO_4 is not stable during the photocatalytic process because of photocorrosion, meaning that in the absence of an electron acceptor, the photogenerated electron decomposes Ag_3PO_4 on photoillumination.[16-18] More recently, $Ag_3PO_4/BiPO_4$-based heterostructures were prepared as a modification of Ag_3PO_4.[19-21] For example, a $BiPO_4@Ag_3PO_4$ core/shell heterojunction photocatalyst was synthesized using a facile hydrothermal process, followed by the ion-exchange method.[19] The results showed that RhB was almost completely degraded in 60 min under visible light irradiation and in 40 min under solar irradiation. The $BiPO_4@Ag_3PO_4$ core/shell

heterojunction photocatalyst exhibited enhanced photocatalytic activity against RhB, which is attributed to the effective charge separation by the core/shell heterojuction between Ag_3PO_4 and $BiPO_4$. One-step synthesis of a $Ag/Ag_3PO_4/BiPO_4$ double-heterostructured photocatalyst was demonstrated by the Lv group.[20] Higher photocatalytic activity and stability for the photodegradation of organic compounds (rhodamine B, RhB) were observed under visible light (98% RhB degradation, 60 min) because of both the formation of an effective heterostructure and the Schottky barrier effect. These two aspects contributed to the charge transfer between the metal and semiconductor and the separation of photogenerated electron–hole pairs; however, this research lacked the experimental evidence to prove these two suggestions. $Ag_3PO_4/BiPO_4$ was synthesized using the co-precipitation hydrothermal method.[21] The higher photocatalytic activity of $Ag_3PO_4/BiPO_4$ (97% methyl orange (MO) degradation, 30 min) could be mainly attributable to strong visible light absorption and a high separation efficiency of electron–hole pairs. However, the stability study was not addressed. Notably, few photocatalytic results have demonstrated the practicability of the aforementioned $Ag_3PO_4/BiPO_4$ photocatalysts.

This paper presents a systematic study of $Ag/Ag_3PO_4/BiPO_4$ synthesis under hydrothermal conditions at 180 °C for 24 h and then calcination at 500 °C for 6 h. The photocatalytic activity, recyclability, and practicability of the synthesized $Ag/Ag_3PO_4/BiPO_4$ were evaluated according to its ability to degrade methylene blue (MB), RhB, and MO in various water samples under visible light ($\lambda > 420$ nm) and solar irradiation. The mechanism of the photocatalytic degradation of organic pollutants by $Ag/Ag_3PO_4/BiPO_4$ was also investigated.

Experimental

Chemicals

All chemicals used were of an analytical grade and of the highest purity available. $AgNO_3$, $Bi(NO_3)_3{\cdot}5H_2O$, Na_3PO_4, MB, RhB, MO, and HNO_3 were purchased from Sigma Aldrich (St. Louis, MO, USA). Milli-Q ultrapure water was used in all of the experiments.

Preparation

$Ag/Ag_3PO_4/BiPO_4$ was synthesized using the impregnation method. First, $Bi(NO_3)_3{\cdot}5H_2O$ (1.25 mmol) and Na_3PO_4 (2.5 mmol) were placed in a beaker. Deionized water (46 mL) and HNO_3 (4 M, 1 mL) were added to the beaker, and the mixture was magnetically stirred to form a homogeneous solution at room temperature. After 1 min, the white precipitate was transferred to a Teflon-lined stainless steel autoclave and maintained at 180 °C for 24 h. A white $BiPO_4$ powder was obtained through centrifugation, washed three times with deionized water and ethanol, and then dried in a desiccator at 55 °C for 12 h. An appropriate amount of $AgNO_3$ was then dissolved in 2 mL of distilled water, and the obtained $BiPO_4$ powder (0.3 g) was dispersed in the $AgNO_3$ solution with magnetic stirring to yield a uniform precursor. The precursor was then maintained at 80 °C for 10 h for the water to evaporate. Finally, the powder obtained was calcined at 500 °C for 6 h to produce $Ag/Ag_3PO_4/BiPO_4$ heterostructures. Herein, various Ag^+ to $BiPO_4$ powder mass ratios, from 0, 3, 6, 15, to 30%, were used to prepare $Ag/Ag_3PO_4/BiPO_4$. We use X% $Ag/Ag_3PO_4/BiPO_4$ to represent the different photocatalysts (X = 3, 6, 15, and 30).

Ag/Ag_3PO_4 samples were synthesized using a precipitation–hydrothermal process. The typical preparation was as follows: $AgNO_3$ (1.25 mmol) and Na_3PO_4 (2.5 mmol) were placed in a beaker. Deionized water (46 mL) and HNO_3 (4 M, 1 mL) were added to the beaker, and the mixture was magnetically stirred to form a homogeneous solution at room temperature. After 1 min, the yellow precipitate was transferred to a Teflon-lined stainless steel autoclave and maintained at 180 °C for 24 h. Yellow Ag/Ag_3PO_4 powders were obtained through centrifugation, washed three times with deionized water and ethanol, and then dried in a desiccator at 55 °C for 12 h.

Characterization

X-ray powder diffraction (XRD) was performed on a LabX XRD-6000 X-ray diffractometer (SHIMADZU, Kyoto, Japan) with Cu Kα radiation ($\lambda = 0.15418$ nm). Raman spectra were measured at room temperature using a confocal micro-Raman system (Thermo Scientific Inc., NY, USA). A 532 nm laser line was used as the photoexcitation source with a laser power of 2 mW focused on the sample for 10 s. FT-IR spectra were collected at room temperature using an Agilent Cary 600 Series FT-IR (Agilent Technologies, Santa Clara, CA, USA). X-ray photoelectron spectroscopy (XPS) measurements were performed using a VG ESCA210 electron spectroscope (VG Scientific, West Sussex, UK). Scanning electron microscopy (SEM) images were obtained using a Hitachi S4300 SEM (Hitachi, Tokyo, Japan) operating at 15 kV. Transmission electron microscopy (TEM) images were recorded using a JEOL-1200EX II TEM (JEOL, Tokyo, Japan) at an accelerating voltage of 200 kV. UV–Vis diffuse reflectance spectra (DRS) were recorded on a UV–Vis spectrometer (Evolution 200, Thermo Fisher, NY, USA) using $BaSO_4$ as a reference. The Brunauer–Emmett–Teller (BET) specific surface areas of the samples were characterized using a PMI C-BET 201A system (USA).

Photocatalytic activity

The photocatalytic activity of the as-prepared photocatalysts (0%–30% mass ratios of Ag^+ to $BiPO_4$) was evaluated for MB degradation under visible light irradiation ($\lambda > 420$ nm, 150 W) by using a Xe lamp as the light source. In these experiments, as prepared photocatalyst (0.2 g) was added to an aqueous MB solution (50 mL, 5 mg/L) in a reactor at room temperature. Prior to irradiation, the solution was stirred for 10 min in the dark to ensure an adsorption–desorption equilibrium. The solution was then exposed to Xe lamp irradiation (150 W) with magnetic stirring. At each designated time interval, 1 mL of the suspension was sampled and centrifuged to remove the

photocatalyst powder. The MB concentration during degradation was monitored using colorimetry with a Synergy H1 Hybrid Multi-Mode Microplate Reader (Biotek Instruments, Winooski, VT, USA). All measurements were performed at room temperature. The photocatalytic degradation conditions of titania P25 (TiO_2, ca. 80% anatase, and 20% rutile), $BiPO_4$, and 15%$Ag/Ag_3PO_4/BiPO_4$ for the various pollutants (MB, RhB, and MO) were the same as described previously, except for the use of solar irradiation. The molecule structure of MB, RhB, and MO are provided in the supporting information (Figure S1).

Detection of methylene blue degradation in real samples

Pond water samples were collected from the campus of National Changhua University of Education, Taiwan. An industrial wastewater sample was collected from a factory near the campus. A seawater sample was collected from a beach in Taichung City. After the real samples were filtered through a 0.2 μm membrane, 15%$Ag/Ag_3PO_4/BiPO_4$ (0.2 g) was added to an aqueous MB solution (50 mL, 5 mg/L) in a reactor at room temperature. Prior to irradiation, the solution was stirred for 10 min in the dark to ensure an adsorption–desorption equilibrium. The solution was then exposed to solar irradiation with magnetic stirring. Experimental time using solar irradiation was performed between 1100 AM and 0200 PM. At each designed time interval, 1 mL of the suspension was sampled and centrifuged to remove the 15%$Ag/Ag_3PO_4/BiPO_4$ powder. The MB concentration during degradation was monitored using colorimetry with a Synergy H1 Hybrid Multi-Mode Microplate Reader.

Photocatalytic disinfection

To evaluate the photocatalytic disinfection of the samples, *E coli* cells using as the model waterborne pathogens were inoculated in phosphate buffer solution (0.2 M, pH 7.2) containing 2 μg L^{-1} 15%$Ag/Ag_3PO_4/BiPO_4$ with a final cell concentration of ~ 10^3 cfu mL^{-1}. The mixture solutions were kept under sunlight irradiation. At each designed time interval, the mixture was applied uniformly on three Luria-Bertani culture medium plates. These plates were incubated at 37 °C for 48 h. The colony forming units were counted and compared with control plates to calculate percentage of cell viability (n/n_0). Control experiments without samples were also carried out at the same time.

Detection of photogenerated electrons, holes, and hydroxyl radical species

To detect photogenerated electrons, $BiPO_4$ and 15%$Ag/Ag_3PO_4/BiPO_4$ films were deposited on indium tin oxide (ITO)-conducting glass for electrochemical measurements. The clean ITO glass substrates were immersed in a slurry of the as-prepared photocatalyst (3 mg) and ethanol (3 mL) mixtures. The substrate was then dried at 80 °C to eliminate ethanol and was subsequently maintained at 80 °C for 6 h.

The experimental procedure followed for examining holes and hydroxyl radical species was similar to that for the photocatalytic activity experiment.[22] Various quantities of scavengers were introduced into the MB solution prior to the addition of the catalyst. In addition, a photoluminescence (PL) technique, with coumarin (1 mM) as a probe molecule, was used to investigate the formation of hydroxyl radicals on the surface of the photocatalysts ($BiPO_4$ and 15%$Ag/Ag_3PO_4/BiPO_4$) illuminated by visible light irradiation for 15 min.[22]

Results and discussion

Phase structure and morphology

XRD analysis was used to identify the phases and purity of the products. Figure 1(a) shows the XRD pattern of $BiPO_4$, which is consistent with the standard data for pure monoclinic $BiPO_4$ (JCPDS 80-0209). Ag/Ag_3PO_4 was prepared under precipitation–hydrothermal conditions, and high temperatures have been reported to favor the reduction of Ag^+ to Ag.[23, 24] The main diffraction peaks of Ag/Ag_3PO_4 could be primarily indexed to the body-centered cubic structure of Ag_3PO_4 (JCPDS 06-0505). The diffraction peaks at 38.1°, 44.3°, and 64.5°, corresponding to (111), (200), and (220) crystal planes of cubic Ag (JCPDS 65-2871), were also obvious. For the $Ag/Ag_3PO_4/BiPO_4$ heterostructure, the coexistence of $BiPO_4$ and Ag/Ag_3PO_4 phases, which are marked with • and □, respectively, could be observed. Similarly, the peaks of the Ag metal, which are marked with ▼, were also obvious.

Figure 1(b) shows the UV-DRS spectra of Ag/Ag_3PO_4, $Ag/Ag_3PO_4/BiPO_4$, and $BiPO_4$. Clearly, yellow Ag/Ag_3PO_4 possessed strong visible light absorption ability, whereas white $BiPO_4$ possessed UV light absorption ability. $Ag/Ag_3PO_4/BiPO_4$ exhibited absorption properties that were a mixture of those of Ag/Ag_3PO_4 and $BiPO_4$. For semiconductor materials, the square of the absorption coefficient was linearly correlated with the energy for direct optical transitions in the absorption edge region, whereas the square root of the absorption coefficient was linearly correlated with the energy for indirect transitions. Data plots of the square root of the absorption coefficient versus the energy in the absorption edge region are shown in the inset of Figure 1(b); the plots are approximately linear. These results suggested that the absorption edges of the three materials were because of indirect transitions; thus, the bandgap energies of the samples were estimated from the plots using the intercept of the tangent to the x-axis. The estimated bandgaps of as-synthesized Ag/Ag_3PO_4, $Ag/Ag_3PO_4/BiPO_4$, and $BiPO_4$ were approximately 2.08, 2.05, and 4.08 eV, respectively (inset of Figure 1(b)). These results clearly confirm that the electronic structures of the as-synthesized materials differ. The variation in the bandgap may be due to different degrees of delocalization and mobility of the photoinduced electron–hole pairs, which may have also resulted in different photocatalytic efficiencies.

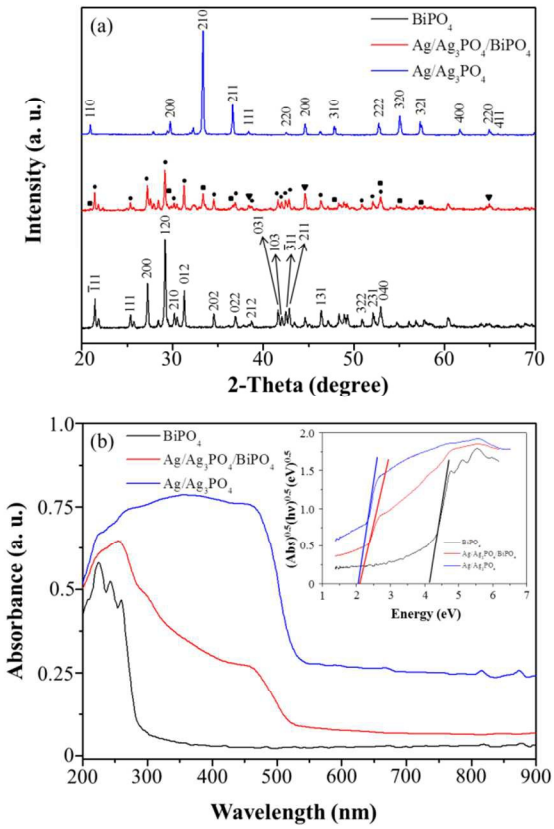

Figure 1. (a) X-ray powder diffraction (XRD) and (b) UV-diffuse reflectance spectra (DRS) of as-prepared $BiPO_4$, $Ag/Ag_3PO_4/BiPO_4$, and Ag/Ag_3PO_4. Inset presents the corresponding $(Abs)^{0.5}(hv)^{0.5}$ versus energy curves.

The structures of Ag/Ag_3PO_4, $Ag/Ag_3PO_4/BiPO_4$, and $BiPO_4$ were further characterized using Raman spectroscopy in the 100–1200 cm^{-1} region (Figure S2A). Notably, the Raman bands we observed in these spectra were consistent with literature data.[25] For $Ag/Ag_3PO_4/BiPO_4$ and $BiPO_4$, the peaks between 100 and 300 cm^{-1} may be assigned to the symmetric bending vibration of the Bi–O bonds. One of the strong features of Raman spectroscopy is that bands below 400 cm^{-1} are readily observed. Thus, the intense bands attributable to M–O bond vibrations could be observed. However, Ag/Ag_3PO_4 exhibited no peaks in this region. For $Ag/Ag_3PO_4/BiPO_4$ and $BiPO_4$, the Raman bands between 460 and 600 cm^{-1} in the spectra in Figure S2 were attributed to the v_4 bending modes of the PO_4 units, and those between 380 and 460 cm^{-1} were attributed to the v_2 bending modes of the PO_4 units. Ag/Ag_3PO_4 exhibited weak peaks corresponding to v_2 and v_4 bending vibrations of the PO_4^{3-} moiety at 408 and 552 cm^{-1}, respectively. The two intense bands between 960 and 1100 cm^{-1} were ascribed to the v_1 symmetric and v_3 antisymmetric stretching modes of the PO_4 tetrahedron in case of $Ag/Ag_3PO_4/BiPO_4$ and $BiPO_4$, respectively. Ag/Ag_3PO_4 exhibited an intense peak at 908 cm^{-1}, which was attributed to the symmetric stretching mode of the PO_4^{3-} moiety under cubic symmetry. A similar peak was also observed in case of $Ag/Ag_3PO_4/BiPO_4$, indicating the presence of the Ag_3PO_4 structure.

FTIR spectroscopy was also used to investigate the structures of the catalysts (Figure S2B). There are four asymmetric stretching (v_3) vibrations of P–O bond resulting from the distortion of tetrahedral phosphate groups in monoclinic $BiPO_4$. These bands are seen at 1070, 1010, 956, and 925 cm^{-1} in the as prepared $BiPO_4$. The asymmetric bending (v_4) vibrations of PO_4 group appeared between 500 to 600 cm^{-1}. These bands appeared at 596, 566, 555, and 528 cm^{-1}, respectively. In the case of as-prepared $Ag/Ag_3PO_4/BiPO_4$, the different relative intensities and wavenumber shifts of the v_3 and v_4 vibration indicate that a slight change in the structure of the PO_4 tetrahedron.[25]

To further investigate the chemical and bonding environment of $Ag/Ag_3PO_4/BiPO_4$ heterostructures, an XPS analysis was performed; the results are shown in Figure S3, where the C 1s peak at 285 eV serves as a calibration standard. In this figure, peaks from Bi, P, O, and Ag could be observed, thus proving the chemical composition of the heterostructures. Both the Bi and Ag bands exhibited distinct doublets because of spin–orbit coupling. The peaks at 159.8 and 164.8 eV were due to $Bi4f_{7/2}$ and $Bi4f_{5/2}$ levels in $BiPO_4$, respectively. The peaks at 442.8 and 465.8 eV corresponded to $Bi3d_{5/2}$ and $Bi3d_{3/2}$ levels in $BiPO_4$, respectively. The peak at 132.8 eV corresponded to P^{5+} in the PO_4^{3-} of $BiPO_4$, while those at 367.8 eV and 373.8 eV corresponded to $Ag3d_{5/2}$ and $Ag3d_{3/2}$, respectively. According to literature,[19, 26] the peak shift (6 eV) between $Ag3d_{5/2}$ and $Ag3d_{3/2}$ is in agreement on that of bulk Ag ($Ag3d_{5/2}$, 368.2 eV; $Ag3d_{3/2}$, 374.2 eV), indicating the appearance of zero-valent Ag in the $Ag/Ag_3PO_4/BiPO_4$ heterostructure.[19, 26]

Figure 2 displays typical SEM and TEM images of $BiPO_4$ and $Ag/Ag_3PO_4/BiPO_4$ products prepared with an increasing Ag content (mass ratios of 3%, 15%, and 30%). Marked differences in the morphology and size of the as-prepared products can be clearly seen in these images. The $BiPO_4$ comprises rod-like nanostructures (Figure 2). The morphology and size of $BiPO_4$ particles were further examined using TEM. The particles had diameters of 180.9 ± 49.3 nm and lengths of 2169.4 ± 257.0 nm. In a typical process for synthesis of $BiPO_4$, $Bi(NO_3)_3{\cdot}5H_2O$ and Na_3PO_4 was mixed with Milli-Q water in the presence of 4 M of HNO_3. The mixture was stirred gently at room temperature for 1 min, at which time the white precipitate was formed, indicating the formation of small $BiPO_4$ NPs. Then the white precipitate was transferred to a Teflon-lined stainless steel autoclave and maintained at 180 °C for 24 h. In the hydrothermal process, the primary particles may aggregate in an oriented fashion, resulting in the formation of a larger single crystal, or they may randomly aggregate and reorient.[10] However, this aggregation-growth mechanism provides a route for the incorporation of defects; numerous cracks were observed on the surface in the HR-TEM image (Figure 2(a)). In the HRTEM image of $BiPO_4$, majority of the particles appeared to be composed of many primary building block particles ranging in size from less than 5 to 10 nm. It is thus assumed in

$BiPO_4$ rod-like structures that the primary particles aggregated in an oriented fashion, producing assemblies of oriented nanoparticles that subsequently underwent further growth.

$Ag/Ag_3PO_4/BiPO_4$, which was impregnated with 3% Ag^+, comprises irregular rod-like nanostructures with diameters of 195.6 ± 70.0 nm and lengths of 1625.7 ± 195.3 nm. As the $BiPO_4$ reacted with water, the hydroxyl groups are generated on the surface of $BiPO_4$ and produced chemical bonding with Ag^+ ions.[19] Through ion exchange process, Ag_3PO_4 particles would be formed on the cracks of $BiPO_4$ surface, as a result short and irregular rod-like heterojunction nanostructures were produced (HR-TEM image in Figure 2(b)). When the Ag^+ content was increased to 15%, short rod-like $Ag/Ag_3PO_4/BiPO_4$ particles with diameters of 171.7 ± 62.1 nm and lengths of 1252.6 ± 159.2 nm were formed. From the HR-TEM image of $15\%Ag/Ag_3PO_4/BiPO_4$, the resolved lattice spacing was determined to be 0.131 and 0.249 nm, which is consistent with the d spacing of the (421) plane of the body-centered cubic phase of Ag_3PO_4 and the $(\bar{3}11)$ plane of the monoclinic phase of $BiPO_4$, respectively. Finally, adding 30% Ag^+ to $BiPO_4$ resulted in shorter rod-like $Ag/Ag_3PO_4/BiPO_4$ structures with diameters of 182.8 ± 54.2 nm and lengths of 853.8 ± 79.2 nm. The HR-TEM image of $30\%Ag/Ag_3PO_4/BiPO_4$ indicated the existence of a distinct lattice spacing of 0.465 nm, which corresponds to the (011) crystal plane of $BiPO_4$.

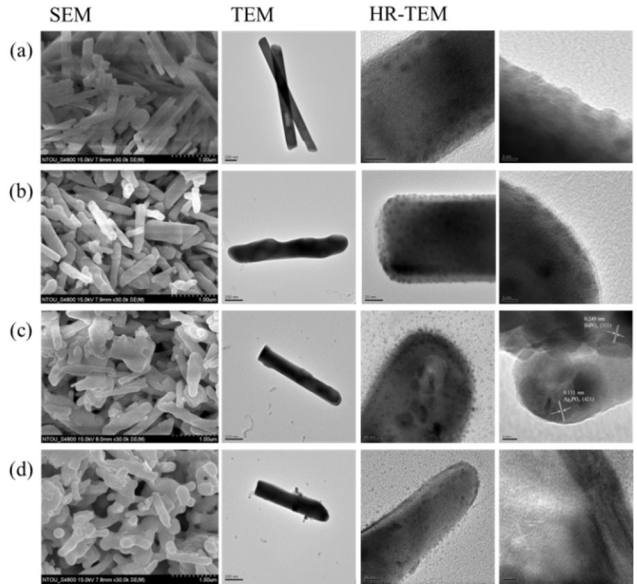

Figure 2. Scanning electron microscopy (SEM), Transmission electron microscopy (TEM), and HR-TEM images of (a) $BiPO_4$, (b) $3\%Ag/Ag_3PO_4/BiPO_4$, (c) 15% $Ag/Ag_3PO_4/BiPO_4$, and (d) 30% $Ag/Ag_3PO_4/BiPO_4$.

The BET specific surface areas of the $BiPO_4$ and $X\%Ag/Ag_3PO_4/BiPO_4$ samples (X = 3, 6, 15, and 30) were also determined using nitrogen adsorption–desorption measurements and the corresponding values are listed in Table 1. As shown in Table 1, the BET surface areas values increases with increasing the amount of Ag^+. Therefore, $BiPO_4$ with Ag^+ impregnation is expected to have higher adsorption capacity and photocatalytic activity for the degradation of dye in water.

Photocatalytic properties

The photocatalytic performance of the as-prepared $BiPO_4$ and $X\%Ag/Ag_3PO_4/BiPO_4$ samples (X = 3, 6, 15, and 30) was evaluated for MB degradation under visible light irradiation. Figure 3(a) presents plots of the variation in the MB concentration (C/C_0) with the irradiation time for the series of $BiPO_4$ and $X\%Ag/Ag_3PO_4/BiPO_4$ photocatalysts, where C_0 is the initial MB concentration, and C is the MB concentration at time t. For comparison, the direct photolysis of MB in the absence of photocatalysts was also analyzed under identical conditions. Clearly, in the absence of photocatalysts, the MB concentration barely changed with an increase in the reaction time, indicating that the as-prepared $Ag/Ag_3PO_4/BiPO_4$ samples are active photocatalysts. In addition, Figure 3(a) shows remarkable differences in the extent of MB degradation within the 15 min observation time of the various $Ag/Ag_3PO_4/BiPO_4$ samples. On further increasing the proportion of Ag^+ more than 15%, the degradation activity did not increase obviously. In this study, $15\%Ag/Ag_3PO_4/BiPO_4$ was found to be the optimal photocatalyst. The photocatalytic degradation kinetics for MB was then investigated (Figure 3(b)), and the photodegradation process was found to be a pseudo first-order reaction. Using the data in Figure 3(b), the pseudo first-order rate constants (k) for MB degradation catalyzed by $BiPO_4$ and the $X\%Ag/Ag_3PO_4/BiPO_4$ samples (X = 3, 6, 15, and 30) were estimated to be 0.0347, 0.0538, 0.1021, 0.2593, and 0.2546 min^{-1}, respectively. Clearly, the rate constant for $15\%Ag/Ag_3PO_4/BiPO_4$ is almost 7.5 times higher than that for $BiPO_4$. The pseudo first-order kinetic equation, rate constants and relative coefficients are summarized in Table 1.

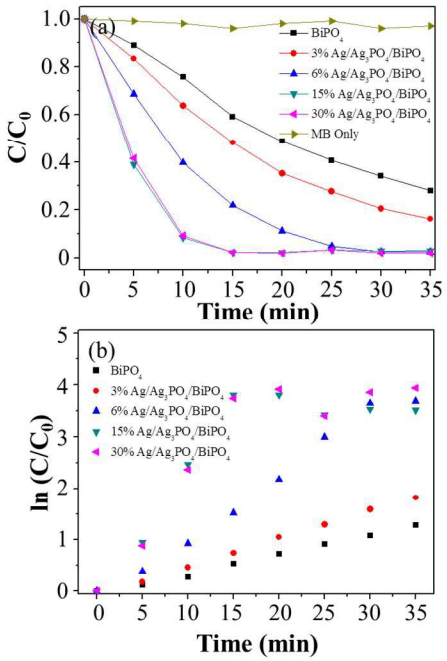

Figure 3. (a) Photocatalytic decomposition curves for MB and (b) kinetic fit for MB degradation catalyzed by $BiPO_4$ and $Ag/Ag_3PO_4/BiPO_4$.

Table 1. Pseudo first-order rate constants for methylene blue photocatalytic oxidation using $BiPO_4$ and $Ag/Ag_3PO_4/BiPO_4$

Series	Pseudo first-order kinetic equation	R^2	Surface area (m^2g^{-1})
$BiPO_4$	y = 0.0347x − 0.0306	0.9720	3.5 ± 0.1
3%$Ag/Ag_3PO_4/BiPO_4$	y = 0.0538x − 0.0538	0.9977	30.1± 0.1
6%$Ag/Ag_3PO_4/BiPO_4$	y = 0.1021x − 0.0609	0.9903	42.5± 0.3
15%$Ag/Ag_3PO_4/BiPO_4$	y = 0.2593x − 0.1372	0.9919	55.1± 0.1
30%$Ag/Ag_3PO_4/BiPO_4$	y = 0.2546x − 0.1072	0.9892	70.1± 0.1

Figure S4(a) and (b) show the temporal evolution of the spectral change upon MB degradation over $BiPO_4$ and 15%$Ag/Ag_3PO_4/BiPO_4$, respectively. According to literature, chromophore cleavage is analogous to a competitive photodegradation reaction involved in the photocatalytic decomposition of organic pollutants.[26] The absorption of MB at 665 nm decreased with an increase in the irradiation time. Moreover, the characteristic absorption of MB in the presence of $BiPO_4$ and 15%$Ag/Ag_3PO_4/BiPO_4$ decreased only insignificantly and exhibited a slight hypsochromic shift. Thus, the cleavage of the MB chromophore is inferred to predominate in both $BiPO_4$ and 15%$Ag/Ag_3PO_4/BiPO_4$ photocatalytic decomposition systems.

Stability evaluation and applications

In addition to the photocatalytic efficiency, the stability of photocatalysts is crucial for practical applications. Therefore, to evaluate the stability and efficiency of the photocatalytic performance of 15%$Ag/Ag_3PO_4/BiPO_4$, a circulating run was performed for MB photocatalytic degradation. Notably, the photocatalytic activity of 15%$Ag/Ag_3PO_4/BiPO_4$ for MB photodegradation did not considerably decrease even after five cycles (Figure S5(a)). Specifically, the MB photocatalytic degradation efficiency still reached 95% after five cycles, indicating that the photocatalyst has good stability, which was confirmed by a lack of change in the XRD pattern for 15%$Ag/Ag_3PO_4/BiPO_4$, after being used for five reaction cycles (Figure S5(b)). These results suggest that with its high catalytic activity and stability, 15%$Ag/Ag_3PO_4/BiPO_4$ should be attractive as a photocatalyst.

To further investigate the photocalalytic activity of the various photocatalysts (P25, $BiPO_4$, Ag/Ag_3PO_4, and 15%$Ag/Ag_3PO_4/BiPO_4$), RhB, MO, and MB degradation under solar irradiation was analyzed; the results are shown in Figure 4(a). 15%$Ag/Ag_3PO_4/BiPO_4$ exhibited excellent photocatalytic activity than that of the P25 and $BiPO_4$ photocatalyst under solar irradiation for the degradation of all dyestuffs, with nearly 100% degradation achieved in only 5 min. This may be because of absorption in the visible region of sunlight. In addition, we found 15%$Ag/Ag_3PO_4/BiPO_4$ could also be easily recovered by sedimentation due to high density of Ag_3PO_4 (6.37 gcm^{-3}) comparing to $BiPO_4$ (6.32 gcm^{-3}) and TiO_2 (4.23 gcm^{-3}), which is beneficial for the applications in water purification. Although the Ag/Ag_3PO_4 also exhibited the similar photocatalytic activity to that of the 15%$Ag/Ag_3PO_4/BiPO_4$ due to high absorption in the visible region of sunlight, the amount of $AgNO_3$ for the preparation of the Ag/Ag_3PO_4 (0.21 g) is more than that of the 15%$Ag/Ag_3PO_4/BiPO_4$ (0.045 g) photocatalyst. This 15%$Ag/AgP_3O_4/BiPO_4$ photocatalyst possesses attractive features (low cost) when compared with Ag/Ag_3PO_4 heterostructures. According to literatures, long UV irradiation also effectively induces electron–hole separation in the $BiPO_4$.[4, 10, 12] This can further improve the photocalytic activity of 15%$Ag/Ag_3PO_4/BiPO_4$ for the practical applications.

To further test the practicality of 15%$Ag/Ag_3PO_4/BiPO_4$, the photocatalytic performance was evaluated for MB degradation in environmental water samples under solar irradiation. Figure 4(b) presents variations in the MB concentration (C/C_0) with the time of irradiation over 15%$Ag/Ag_3PO_4/BiPO_4$, where C_0 is the initial MB concentration and C is the MB concentration at time t. For all of the environmental water samples, in the presence of 15%$Ag/Ag_3PO_4/BiPO_4$, the MB concentration decreased with an increase in the reaction time, indicating that the as-prepared material is an active photocatalyst. A remarkable difference in MB degradation with time was observed for the pond water (within 5 min) than that for the seawater and industrial wastewater (within 20 min). This may be because anions or radical scavengers in the seawater and industrial wastewater samples reduced the photocatalytic activity of 15%$Ag/Ag_3PO_4/BiPO_4$. Further research on the high photocatalytic activity of other heterojunction $BiPO_4$ composites, such as those enwrapped by graphene oxide and carbon nanotubes, is now underway in our laboratory.[27-31]

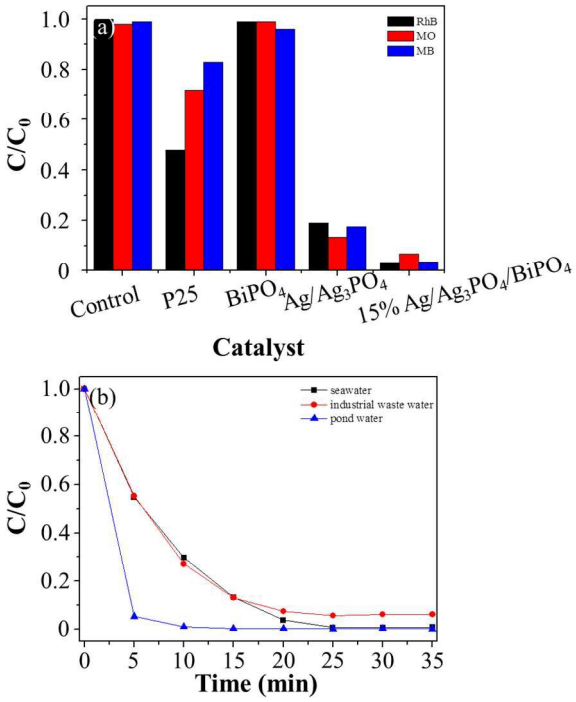

Figure 4. (a) Photocatalytic activities of P25, $BiPO_4$, Ag/Ag_3PO_4, and 15%$Ag/Ag_3PO_4/BiPO_4$ for rhodamine B (RhB), methyl orange (MO), and MB degradation under solar irradiation (5 min) and (b) photocatalytic activities of 15%$Ag/Ag_3PO_4/BiPO_4$ for MB degradation in different environmental water samples under solar irradiation.

Next, to test the microorganism disinfection ability, the photocatalytic disinfection of 15%Ag/Ag_3PO_4/$BiPO_4$ was evaluated using the model waterborne pathogen *E. coli*. Figure 5(a) presents plots of the variation in the *E. coli* colony forming units (n/n_0) with the irradiation time for the control and 15%Ag/Ag_3PO_4/$BiPO_4$, where n_0 is the initial *E. coli* colony forming units, and n is the *E. coli* colony forming units at time t. It shows that 90% *E. coli* removal occurred in the presence of 15%Ag/Ag_3PO_4/$BiPO_4$ under sunlight irradiation for 30 min. The bactericidal activity of the sample is also confirmed by the images of colonies incubated on an agar plate the control and 15%Ag/Ag_3PO_4/$BiPO_4$ under sunlight irradiation (image d and e in the Figure 5). Interesting, 15%Ag/Ag_3PO_4/$BiPO_4$ also presents the intrinsic antibacterial activity in the dark condition for 30 min (about 40% *E. coli* cell removal, shown in the Figure 5(a), image b and c in the Figure 5). As we known, Ag-based composites are to be effective biocides against many bacteria.[31] Thus, it is reasonable to suggest that the Ag/Ag_3PO_4/$BiPO_4$ could be used for the disinfection applications.

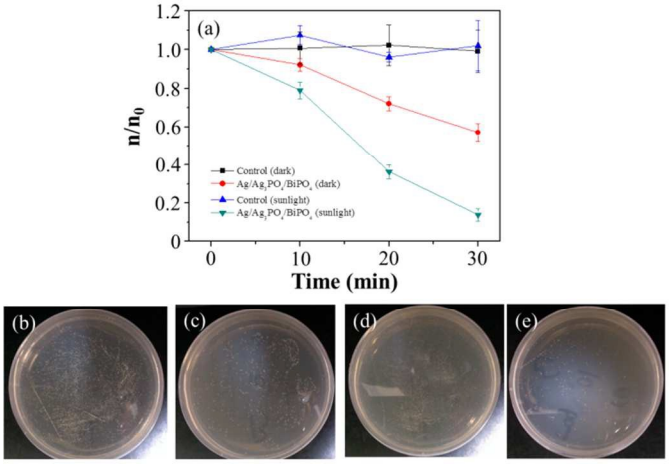

Figure 5. (a) Photocatalytic disinfection activity of the control and 15%Ag/Ag_3PO_4/$BiPO_4$ for E. coli cells with and without solar irradiation. Each data point and error bar represents the mean and the standard errors (n = 3). Images of E. coli colonies on an agar plate under different conditions: (b) the control and (c) 15%Ag/Ag_3PO_4/$BiPO_4$ in the dark, (d) the control and (e) 15%Ag/Ag_3PO_4/$BiPO_4$ with solar irradiation for 30 min.

Photocatalytic mechanism

The higher separation efficiency and lower recombination rate of the photogenerated electrons and holes are the major factors that contribute to the increased photocatalytic activity of 15%Ag/Ag_3PO_4/$BiPO_4$. We proved our suggestions by conducting the following photocurrent and PL experiments.

First, the photocurrent responses of $BiPO_4$ and 15%Ag/Ag_3PO_4/$BiPO_4$ were measured to reflect the separation efficiency of the photogenerated electrons and holes. Uniform photocurrent responses to the light were detected (Figure S6(a)). In addition, the photocurrent response of 15%Ag/Ag_3PO_4/$BiPO_4$ was higher than that of $BiPO_4$ (three times), indicating enhanced separation of photogenerated electrons and holes. Moreover, a heterostructure was formed between Ag and Ag_3PO_4 nanoparticles. Such heterostructures can also improve the separation of photogenerated electrons and holes through the Schottky barrier effect, which is consistent with a previous study on electron transfer from a semiconductor to a metal.[20] Ag nanoparticles on the Ag_3PO_4 surface act as absorbents for electrons; this contributes to the interfacial charge transfer between the metal and semiconductor and to the separation of photogenerated electrons and holes, thus enhancing the photocatalytic activity.

The recombination of electron–hole pairs can release energy in the form of PL emission. A low electron–hole recombination rate implies a lower luminescence emission intensity and higher photocatalytic activity.[9] Thus, to understand the recombination rates of the electron–hole pairs during photocatalysis using $BiPO_4$ and 15%Ag/Ag_3PO_4/$BiPO_4$, the PL emission spectra of the samples were measured at λ_{ex} = 250 nm (Figure S6(b)). The emission intensity of $BiPO_4$ was greater than that of 15%Ag/Ag_3PO_4/$BiPO_4$, indicating that the electron–hole pairs in $BiPO_4$ recombine rapidly. As mentioned earlier, the heterostructure interface between the $BiPO_4$ and Ag_3PO_4 nanoparticles had numerous defects that suppressed the recombination of photogenerated electrons and holes, resulting in increased photocatalytic activity.

Radical- and hole-trapping experiments were designed to elucidate the photocatalytic degradation process for 15%Ag/Ag_3PO_4/$BiPO_4$. Under irradiation, MB photodegradation was suppressed upon the addition of the hole scavenger disodium ethylenediamine tetraacete (EDTA-2Na) but only slightly inhibited upon the addition of the radical scavenger *tert*-butyl alcohol (Figure S7(a)). These results indicate that a hole is the primary active species involved in the decomposition of the adsorbed organic pollutants. Therefore, holes play a crucial role in the Ag/Ag_3PO_4/$BiPO_4$ photocatalytic system. Hydroxyl radicals can be formed through the hole oxidation of OH^- or the reduction of O_2. The former route is controlled by the potential of the holes in the valence band.[32, 33] The effect of using a N_2 atmosphere is shown in Figure S7(b). In an anoxic suspension, MB photodegradation decreased, which indicated that O_2 is also an essential source for the generation of superoxide species and hydroxyl radicals via photoreduction. To further confirm the existence of hydroxyl radicals, $BiPO_4$ and 15%Ag/Ag_3PO_4/$BiPO_4$ illuminated by Xe light were examined using the PL technique. The PL emission spectra, excited at 370 nm in the coumarin solution containing a suspension of $BiPO_4$ or 15%Ag/Ag_3PO_4/$BiPO_4$, were measured after each sample was illuminated for 15 min. Figure S8 shows that a PL signal was observed at 516 nm for each sample. The maximum PL intensity was observed for 15%Ag/Ag_3PO_4/$BiPO_4$. This suggests that the fluorescence was due to chemical reactions of coumarin with hydroxyl radicals formed in the photocatalytic reactions.[22] Hence, the hydroxyl radical is the indirect reactive oxidation species in the Ag/Ag_3PO_4/$BiPO_4$ samples and finally induces MB degradation.

On the basis of the aforementioned discussion, a possible mechanism for the increased photodegradation activity and stability of the Ag/Ag_3PO_4/$BiPO_4$ heterostructures is presented

in Scheme 1. The conduction band (CB) and valence band (VB) positions in $BiPO_4$ and Ag/Ag_3PO_4 were calculated using the equation $E_{VB} = X - E_e + 0.5E_g$, where X is the Mulliken electronegativity (X_{Ag3PO4}: 5.961 ev, X_{BiPO4}: 6.492 ev), E_e is the energy of free electrons on the hydrogen scale (≅ 4.5 eV), and E_g is the bandgap. The E_{VB} for the $BiPO_4$ and Ag_3PO_4 were thus estimated to be 4.032 and 2.486 eV, meanwhile the E_{CB} of them were −0.048 and 0.436 eV, respectively. The illumination energy of sunlight can be efficiently absorbed by $Ag/Ag_3PO_4/BiPO_4$. The electron in the VB can be excited to the CB with simultaneous generation of the same amount of holes in the VB. Because the energy position of the CB of the Ag_3PO_4 is lower than that of the $BiPO_4$, $Ag/Ag_3PO_4/BiPO_4$ heterostructures would produce an interface. Therefore, the generated electrons in CB are limited to immigrate from $BiPO_4$ (electronic barrier) to Ag_3PO_4 (electronic potential well). The generated electron from Ag_3PO_4 and $BiPO_4$ can be quickly reacted with water and oxygen for the generation of superoxide specie. However, superoxide specie is not the primary active species in the decomposition of the adsorbed organic pollutants. The energy level of the VB of the Ag_3PO_4 is higher than that of the $BiPO_4$; the generated holes in VB are thus immigrated from $BiPO_4$ to Ag_3PO_4 in the $Ag/Ag_3PO_4/BiPO_4$ heterostructures, whereas the accumulated holes on Ag_3PO_4 to oxidize organic substances. Therefore, $Ag/Ag_3PO_4/BiPO_4$ suppresses the recombination of electron–hole pairs because of the heterostructure interface. In addition, Ag nanoparticles on the Ag_3PO_4 surface also act as electron acceptors, thus contributing to the separation of photogenerated electron–hole pairs. These two factors enhance the production of active holes and hydroxyl radicals, which decompose MB. Furthermore, excess electrons favor the presence of Ag nanoparticles that also decrease the reduction of Ag^+ of the Ag_3PO_4 photocatalyst, thus increasing the stability of the photocatalyst.[20, 24]

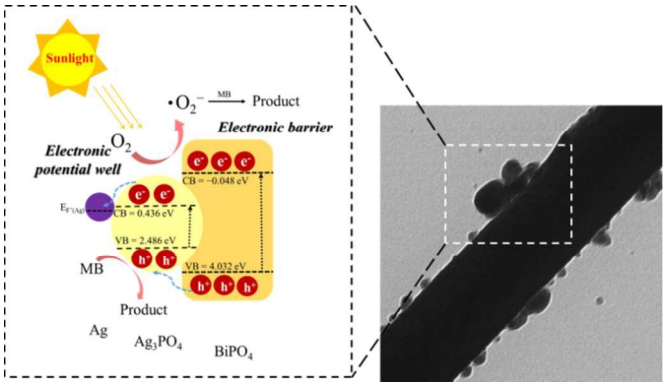

Scheme 1. Proposed mechanism for the MB photocatalytic degradation catalyzed by $Ag/Ag_3PO_4/BiPO_4$.

This novel $Ag/AgP_3O_4/BiPO_4$ photocatalyst possesses several attractive features when compared with different $Ag/Ag_3PO_4/BiPO_4$-based heterostructures (table 2): (1) facile and simplicity—sophisticated preparation process is not required; (2) high stability and photocatalytic performance—95% photocatalytic degradation of various organic dyes (MB, RhB, and MO) is observed within 5 min; (3) practicality—the sunlight induced photocatalytic degradation of dyes in the complicated samples (seawater, pond water, and industrial wastewater samples) and disinfection of *E. coli* cells are possible. Further application research using this novel $Ag/AgP_3O_4/BiPO_4$ photocatalyst, such as water purification and direct methanol fuel cells, is now underway in our laboratory.

Conclusions

$Ag/Ag_3PO_4/BiPO_4$, with controllable morphology and phases, was prepared using a hydrothermal process combined with an impregnation technique, and $15\%Ag/Ag_3PO_4/BiPO_4$ exhibited the highest photocatalytic activities for MB degradation under visible light (15 min) and solar (5 min) irradiation. The high photocatalytic activity and stability of $15\%Ag/Ag_3PO_4/BiPO_4$ were primarily attributed to the high separation efficiency and low recombination of electron–hole pairs. The practicality of $15\%Ag/Ag_3PO_4/BiPO_4$ was validated according to its ability to degrade MB in environmental water samples, demonstrating its photocatalytic activity. Moreover, $15\%Ag/AgP_3O_4/BiPO_4$ also showed sunlight-induced photocatalytic disinfection activity toward *E. coli* cells. Therefore, this study not only presents a possible mechanism of the photocatalytic activity of the $Ag/AgP_3O_4/BiPO_4$ photocatalysts, but also provides evidences for the recyclability and potential for the practical applications of $Ag/AgP_3O_4/BiPO_4$ photocatalyst for the treatment of contaminated wastewater and the environmental water samples.

Acknowledgements

This study was supported by the Ministry of Science and Technology under contract (MOST 101-2113-M-018-001-MY2). We would like to thank anonymous reviewers and the editor for their comments. We thank Wallace Academic Editing for the English language editing.

Journal Name RSCPublishing

ARTICLE

Table 2. Comparing photocatalytic properties, stability, and practicality applications for different $Ag/Ag_3PO_4/BiPO_4$-based heterostructures.

Photocatalyst	Synthesis method	Photocatalytic activity ($\lambda > 420$ nm)	Sunlight irradiation	Stability	Degradation target	Environmental water samples	Ref.
$BiPO_4$@Ag_3PO_4	hydrothermal process and ion-exchange method	95% degradation (0.05 g photocatalyst/20 ppm RhB) within 60 min (500 W)	95% degradation (0.05 g photocatalyst/20 ppm RhB) within 40 min	-[a]	RhB	-[a]	19
$Ag/Ag_3PO_4/BiPO_4$	low temperature chemical bath method	98% degradation (0.1 g photocatalyst/10 ppm RhB) within 60 min (300 W)	-[a]	-[a]	RhB	--[a]	20
$Ag_3PO_4/BiPO_4$	co-precipitation hydrothermal method	97% degradation (0.1 g photocatalyst/10 ppm MO) within 30 min (500 W)	-[a]	3 recycling	MO	-[a]	21
$BiPO_4$:Ag	Sonochemical synthesis	100% degradation (0.03 g photocatalyst/9.6 ppm RhB) within 120 min (150 W)	-[a]	5 recycling	RhB	-[a]	25
$Ag/BiPO_4$	hydrothermal and impregnation processes	90% degradation (0.05 g photocatalyst/3.2 ppm MB) within 20 min (500 W)[b]	-[a]	5 recycling	MB	-[a]	26
$Ag/Ag_3PO_4/BiPO_4$	hydrothermal and impregnation processes	95% degradation (0.2 g photocatalyst/5 ppm MB) within 15 min (150 W)	95% degradation (0.2 g photocatalyst/5 ppm MB) within 5 min	5 recycling	MB, RhB, MO, *E. coli* cell	seawater, pond water, industrial wastewater samples	This study

[a] not provided

[b] mercury lamp with main emission wavelength 313 nm

Notes and references

[a] Department of Chemistry, National Changhua University of Education, Changhua City, Taiwan, ROC.

[b] Graduate Institute of Biotechnology, National Changhua University of Education, Changhua City, Taiwan, ROC.

Electronic Supplementary Information (ESI) available: [Figure S1. Molecular structures of MB, RhB, and MO. Figure S2. XPS spectra of as-prepared $Ag/Ag_3PO_4/BiPO_4$. Figure S3. Temporal evolution of the spectral change upon MB degradation over (a) $BiPO_4$ and (b) $15\%Ag/Ag_3PO_4/BiPO_4$. Figure S4. (a) Cycling runs of MB photocatalytic degradation in the presence of $15\%Ag/Ag_3PO_4/BiPO_4$ products and (b) XRD pattern for $15\%Ag/Ag_3PO_4/BiPO_4$ after being used for five reaction cycles. Figure S5. (a) Photocurrents and (b) PL spectra measured at λ_{ex} = 250 nm of $BiPO_4$ and $15\%Ag/Ag_3PO_4/BiPO_4$. Figure S6. (a) Plots of photogenerated carrier trapping for MB photodegradation catalyzed by $15\%Ag/Ag_3PO_4/BiPO_4$. (b) Effect of O_2 and N_2 on MB photocatalytic degradation in the presence of $15\%Ag/Ag_3PO_4/BiPO_4$. Figure S7. PL spectra of $BiPO_4$ and $15\%Ag/Ag_3PO_4/BiPO_4$ in coumarin solution measured at λ_{ex} = 370 nm (each sample was illuminated for 15 min under visible light).]. See DOI: 10.1039/b000000x/

1. N. N. Mahamuni and Y. G. Adewuyi, *Ultrason. Sonochem.*, 2010, **17**, 990-1003.
2. X. Chen, S. Shen, L. Guo and S. S. Mao, *Chem. Rev.*, 2010, **110**, 6503-6570.
3. A. Fujishima, X. Zhang and D. A. Tryk, *Surf. Sci. Rep.*, 2008, **63**, 515-582.
4. C. Pan and Y. Zhu, *Environ. Sci. Technol.*, 2010, **44**, 5570-5574.
5. M. Muruganandham, R. P. S. Suri, M. Sillanpaa, J. J. Wu, B. Ahmmad, S. Balachandran and M. Swaminathan, *J. Nanosci. Nanotechno.*, 2014, **14**, 1898-1910.
6. S. T. Huang, Y. R. Jiang, S. Y. Chou, Y. M. Dai and C. C. Chen, *J. Mol. Catal. a-Chem.*, 2014, **391**, 105-120.
7. Y. Sang, L. Kuai, C. Y. Chen, Z. Fang and B. Y. Geng, *Acs. Appl. Mater. Inter.*, 2014, **6**, 5061-5068.
8. J. J. Sun, X. Y. Li, Q. D. Zhao, J. Ke and D. K. Zhang, *J. Phys. Chem. C*, 2014, **118**, 10113-10121.
9. S. Y. Wu, H. Zheng, Y. W. Lian and Y. Y. Wu, *Mater Res. Bull.*, 2013, **48**, 2901-2907.
10. L.-W. Cheng, J.-C. Tsai, T.-Y. Huang, C.-W. Huang, B. Unnikrishnan and Y.-W. Lin, *Matter. Res. Exp.*, 2014, **1**, 025023.
11. Y. Y. Zhu, Y. F. Liu, Y. H. Lu, H. Wang, Q. Ling and Y. F. Zhu, *Acta Phys.-Chim. Sin.*, 2013, **29**, 576-584.
12. C. Pan, J. Xu, Y. Chen and Y. Zhu, *Appl. Catal. B-Environ.*, 2012, **115–116**, 314-319.
13. C. S. Pan, D. Li, X. G. Ma, Y. Chen and Y. F. Zhu, *Catal. Sci. Technol.*, 2011, **1**, 1399-1405.
14. S. Kumar, T. Surendar and V. Shanker, *Mater. Lett.*, 2014, **123**, 172-175.
15. X. Z. Li, K. L. Wu, C. Dong, S. H. Xia, Y. Ye and X. W. Wei, *Mater. Lett.*, 2014, **130**, 97-100.

16. J. H. Liu, X. Li, F. Liu, L. H. Lu, L. Xu, L. W. Liu, W. Chen, L. M. Duan and Z. R. Liu, *Catal. Commun.*, 2014, **46**, 138-141.
17. L. Luo, Y. Z. Li, J. T. Hou and Y. Yang, *Appl. Surf. Sci.*, 2014, **319**, 332-338.
18. X. L. Ma, H. H. Li, Y. H. Wang, H. Li, B. Liu, S. Yin and T. Sato, *Appl. Catal. B-Environ.*, 2014, **158**, 314-320.
19. Y. L. Ren, X. Y. Li and Q. D. Zhao, *Chem. J. Chinese. U.*, 2014, **35**, 2435-2441.
20. Y. H. Lv, K. Huang, W. Zhang, B. Yang, F. L. Chi, S. L. Ran and X. G. Liu, *Ceram. Int.*, 2014, **40**, 8087-8092.
21. H. L. Lin, H. F. Ye, B. Y. Xu, J. Cao and S. F. Chen, *Catal. Commun.*, 2013, **37**, 55-59.
22. K.-I. Ishibashi, A. Fujishima, T. Watanabe and K. Hashimoto, *Electrochem. Commun.*, 2000, **2**, 207-210.
23. Y. P. Liu, L. Fang, H. D. Lu, Y. W. Li, C. Z. Hu and H. G. Yu, *Appl. Catal. B-Environ.*, 2012, **115**, 245-252.
24. W. Teng, X. Y. Li, Q. D. Zhao, J. J. Zhao and D. K. Zhang, *Appl. Catal. B-Environ.*, 2012, **125**, 538-545.
25. M. H. Fulekar, A. Singh, D. P. Dutta, M. Roy, A. Ballal and A. K. Tyagi, *Rsc Adv.*, 2014, **4**, 10097-10107.
26. Y. N. Zhang, H. Q. Fan, M. M. Li and H. L. Tian, *Dalton T.*, 2013, **42**, 13172-13178.
27. Z. L. Ai, Y. Z. Wu, X. P. Hao, Q. F. Lu and S. W. Liu, *Mater Res. Bull.*, 2014, **59**, 192-198.
28. B. Chai, J. Li and Q. Xu, *Ind. Eng. Chem. Res.*, 2014, **53**, 8744-8752.
29. C. Cui, Y. P. Wang, D. Y. Liang, W. Cui, H. H. Hu, B. Q. Lu, S. Xu, X. Y. Li, C. Wang and Y. Yang, *Appl. Catal. B-Environ.*, 2014, **158**, 150-160.
30. B. Liu, Z. Y. Li, S. Xu, D. D. Han and D. Y. Lu, *J. Alloy. Compd.*, 2014, **596**, 19-24.
31. L. Liu, J. C. Liu and D. D. Sun, *Catal. Sci. Technol.*, 2012, **2**, 2525-2532.
32. S. Zheng, W. J. Jiang, Y. Cai, D. D. Dionysiou and K. E. O'Shea, *Catal Today*, 2014, **224**, 83-88.
33. S. Zheng, W. J. Jiang, M. Rashid, Y. Cai, D. D. Dionysiou and K. E. O'Shea, *Molecules*, 2015, **20**, 2622-2635.

